Spectrochimica Acta Part A: Molecular and Biomolecular Spectroscopy 358 (2026) 127837

Contents lists available at ScienceDirect

Spectrochimica Acta Part A:
Molecular and Biomolecular Spectroscopy

journal homepage: www.journals.elsevier.com/spectrochimica-acta-part-a-molecular-and-biomolecular-spectroscopy

Flexible disulfide-bridged hyperbranched poly(amido amine)s based nonconjugated carbonized polymer dots for iron (III) sensing and its application in meat by-product

Xiaoxian Tian [a,1], Liang Li [a,d,1], Chaoren Yan [c], Zhenyu Wang [a], Xiaochun Zheng [a], Bai-Tong Liu [b], Li Chen [a], Shaobo Li [a], Mengyu Shang [a], Cheng Li [a,*], Dequan Zhang [a]

[a] Key Laboratory of Agro-products Quality and Safety Control in Storage and Transport Process, Institute of Food Science and Technology, Chinese Academy of Agricultural Sciences, Beijing 100193, China
[b] School of Chemistry, Chemical Engineering and Biotechnology, Nanyang Technological University, 21, Nanyang Link, 637371, Singapore
[c] School of Medicine, Key Laboratory for Molecular Genetic Mechanisms and Intervention Research on High Altitude Disease of Tibet Autonomous Region, Engineering Research Center of Tibetan Medicine Detection Technology Ministry of Education, Joint Laboratory for Research on Active Components and Pharmacological Mechanism of Tibetan Materia Medica of Tibetan Medical Research Center of Tibet, Xizang Minzu University, Xianyang, Shaanxi 712082, China
[d] Laboratory of Chemistry of Natural Molecules, Gembloux Agro-Bio Tech, University of Liege, Passage Des Déportés 2, B-5030 Gembloux, Belgium

HIGHLIGHTS

- A new carbonized polymer dot with flexible disulfide-bridged structure.
- A novel strategy for modulting quantum yield by controllably introducing the disulfide bonds.
- The carbonized polymer dots show selective identification of iron (III).
- A novel technique for real applications in identifying total iron content of meat by-product.

GRAPHICAL ABSTRACT

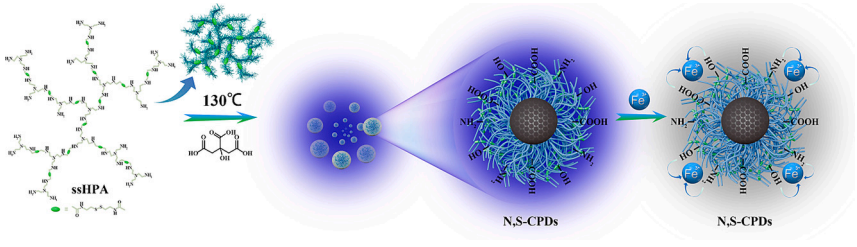

ARTICLE INFO

Keywords:
Carbonized polymer dots
Hyperbranched poly(amido amine)s
Iron, fluorescence
Detection

ABSTRACT

Herein, a novel flexible disulfide-bridged hyperbranched poly(amido amine)s based nonconjugated carbonized polymer dots (ssHPA-CPDs) was developed using citric acid and ssHPA with disulfide bonds as precursors. The structure and composition of ssHPA-CPDs were characterized by transmission electron microscopy, X-ray photoelectron spectroscopy, Fourier transform infrared spectroscopy, raman spectroscopy, and small-X-ray scattering. The results show that when the mass ratio of ssHPA-CPDs/citric acid is 0.5, graphite nitrogen and thiophenone/thiazole sulfur occupy a dominant position, with a higher quantum yield (29.08%). The high disulfide bond content increases ssHPA-CPDs flexibility, leading to greater surface roughness and enhanced Fe(III) binding. In addition, the fluorescence intensity of ssHPA-CPDs at 465 nm (λex = 350 nm) was used as the quantitative signal for Fe(III) detection with a limit of detection of 0.07 μM. The ssHPA-CPDs offering a rapid (1.0 min) and reproducible (three times) method by adding ascorbic acid for accurately determining Fe(III) content in liver and blood samples, with spiked recovery rates ranging from 87.47% to 106.01%. This method

* Corresponding author.
E-mail address: licheng01@caas.cn (C. Li).
[1] These authors contributed to the work equally and should be regarded as co-first authors.

https://doi.org/10.1016/j.saa.2026.127837
Received 5 January 2026; Received in revised form 17 March 2026; Accepted 31 March 2026
Available online 1 April 2026

adopts flexible disulfide-bridged CPDs to regulate quantum yield, offering a rapid and accurate approach to detect Fe(III) content in meat by-products for the evaluation of food safety and human health.

1. Introduction

The iron (Fe) is considered as the indispensable element for life [1,2]. Particularly, the Fe element serves as a critical component of haemoglobin and iron-sulfur clusters, essential for oxygen transport and haematological homeostasis [3,4]. Moreover, iron levels in some tissues serve as key indicators for metabolic diseases [5,6]. The World Health Organization (WHO) recommends that the allowable daily intake of Fe should be 7–18 mg/day, as both insufficient and excessive intake of Fe could lead to serious biological dysfunctions and physiological damage [7–9]. Meat by-products, such as liver and blood, are not only significant in human dietary cultures but also important sources of dietary iron [10,11]. Knowledge of the iron content in animal-derived foods regulates dietary iron balance and safeguards human health. Therefore, it is of great significance to develop a rapid, convenient and accurate method for detecting iron content in meat by-products.

Fluorescent carbon dots (CDs) prove to be one of the most effective tools for Fe (III) sensing due to their low toxicity, distinct optical properties, and excellent light stability [12–14]. Among them, carbonized polymer dots (CPDs), as an essential subgroup of CDs, exhibit enhanced structural stability compared to conventional polymers due to the carbonized framework, and better compatibility due to the retained polymeric chains. For instance, Han et al. [15] prepared highly sensitive and selective CPDs using citric acid, urea, and ammonium paratungstate as raw materials. The CPDs possess a quantum yield of 3.86%, with a good response for Fe (III) sensing. Xia et al. [16] synthesized room temperature-derived CPDs using ascorbic acid and diethylenetriamine. The response to Fe (III) is linear within the concentration range of 0.2 to 10.0 μM, with a LOD of 0.1 μM. However, the challenges such as low quantum yield, high detection limit and so on, still limit its real application.

Hyperbranched polymers with spherical, three-dimensional structures and abundant terminal groups are promising polymer materials for the nonconjugated CPDs synthesis. Such nonconjugated CPDs were first discovered by Yin et al. [17] in 2012. To date, various hyperbranched polymers have been employed as precursors for CPDs synthesis, such as hyperbranched polyethylenimine (PEI), hyperbranched polysiloxane, hyperbranched polyborates, and so on [18,19]. For instance, Zhu et al. [20] and Bhattacharyya et al. [21] adopt branched PEI as a model nonconjugated polymer to investigate its high photoluminescent properties. The results reveal that the enhanced photoluminescence is attributed to Crosslinking-Enhanced Emission (CEE) effect, arising from the restricted vibration and rotation of the crosslinked PEI chains, as well as the numerous sp^2 domains formed alongside graphitic nitrogen. The elements addition (such as N, S, O) by modulating the energy band structure and electronic structure of CPDs can further enhance the crosslinking structure and possess excellent optical properties [22–25]. However, as a commercial product, the flexibility of the three-dimensional structure and the adjustability of its elements of PEI are severely limited, which poses great challenges for further improving the detection performance and fluorescence properties.

To our best knowledge, CPDs derived from hyperbranched poly (amido amine)s incorporating flexible disulfide linkages within their internal architecture have not yet been reported. Moreover, the backbone flexibility modulated by controlled incorporation of disulfide linkages within hyperbranched polymers on the photoluminescent behavior of the resulting CPDs remains unexplored. Herein, we developed a series of disulfide-bridged hyperbranched poly(amido amine)s based on N, S Co-doping ssHPA-CPDs. Through precise adjustment of the content of ssHPA and disulfide group content in ssHPA backbone structures, we successfully developed a system model for CPDs with tunable backbone flexibility. This study proposes an innovative heteroatom doping strategy that utilizes sulfur-enriched hyperbranched poly(amido amine) precursors with gradient disulfide bond concentrations, achieving a remarkable enhancement in QY up to 29.08% in water. After reacting with Fe^{3+}, the luminescence of ssHPA-CPDs can be sharply, sensitively, and selectively reduced via a static quenching mechanism. This sensor has been utilized for measuring trace amounts of Fe (III) content in real samples such as liver and blood. In summary, this method offers the advantages of fast response, convenience, and high sensitivity. Consequently, it holds significant promise for applications in Fe (III) detection within the food analysis and biomedical field.

2. Experimental

2.1. Materials

$FeCl_3$, citric acid (CA), quinine sulfate, ascorbic acid (AA), and methanol (chromatography grade) were purchased from Shanghai Adamasi Reagents Co., Ltd. Cystamine dihydrochloride, tri(2-aminoethyl) amine (TAEA) and acryloyl chloride were purchased from Beijing J&K Scientific Ltd. Dulbecco's Modified Eagle Medium (DMEM), fetal bovine serum (FBS), 3-(4,5-dimethylthiazol-2-yl)-2,5-diphenyltetrazoliumbromid (MTT) were obtained from Jiangsu Sumeike Biological Technology Co. Ltd. All additional employed directly without any further purification. N, N′-cystaminebisacrylamide (CBA) and *N*, *N*′-hexmethylenebisacrylamide (HMBA) were synthesized according to our previous work [26]. Pig and chicken liver were purchased from Xingfu Rongyao Supermarket in Beijing, and pig and duck blood were purchased from Beijing Ershang Xijie Foodstuff Co., Ltd.

2.2. Synthesis of ssHPA

The ssHPAs were synthesized by Michael addition reaction between TAEA and CBA/HMBA, and the different content of disulfide groups in ssHPAs was designed by adjusting the molar ratio of CBA/HMBA, named as $ssHPA_{X\%}$. Typically, the mixture of CBA/HMBA (2.0 mmol in total) dissolved in 2 mL of methanol and TAEA (2.2 mmol) dissolved in 8 mL of methanol was mixed and reacted under N_2 for 96 h. Finally, the polymerization solution was added to the CH_3OH/HCl solution to obtain the product.

2.3. Synthesis of ssHPA-CPDs

For preparation of ssHPA-CPDs, CA (1.0 g) and ssHPAs with different S—S bond content (named as $ssHPA_{x\%}$-CPDs) or different masses (0.04–2.0 g) (named as $ssHPA\text{-}CPD_x$) were dissolved in ultrapure water (100 mL), and then transferred to a polytetrafluoroethylene autoclave and reacted at 130 °C for 6 h in an oven. Once cooled to room temperature, the solution was filtered through a membrane filter (0.22 μm) to obtain the purified product. Subsequently, the final product was obtained through freeze-drying.

2.4. Characterization

The nano-morphology was characterized using a JEM-2200FS transmission electron microscope (Japan). Raman spectroscopy analysis of ssHPA-CPDs was performed by aligning laser beams using a full power 632.8 nm laser source (Melles Griot 05-LHP-991) in combination with a spectrometer (Princeton Instrument Acton SP2500) and a microscope (Zeiss Axio Scope. A1). ^1H NMR spectra of ssHPA-CPDs were measured using a Bruker 400 MHz spectrometer (Germany).

Photoluminescence spectra were acquired with a F-380 spectrofluorometer (China), the fluorescence lifetime was measured using the Edinburgh FLS980 steady-state/transient fluorescence spectrometer (UK), while UV–vis absorption spectra were measured using a Shimadzu UV-1800 spectrophotometer (Japan). X-ray photoelectron spectroscopy (XPS) analysis was performed on a Thermo Scientific ESCALAB 250Xi electron spectrometer (USA). The fourier transform infrared (FT-IR) spectra was obtained by a PerkinElmer Spectrum 100 spectrophotometer (USA). Dynamic light scattering (DLS) and Zeta potential was measured with a Malvern Zetasizer Nano ZS instrument (UK). Model dependent fitting and analysis of Small-X-ray scattering (SAXS), including scattering length density calculation, were performed using SasView (v.4.1.2). DFT calculation was employed to calculate each structure which are optimized by the usage of B3LYP-D3 functional theory with 6-31G(d,p) basis set, and the calculations have been performed using Gaussian 16 program package.

2.5. Fluorescent determination of Fe^{3+} ions

First, the ssHPA-CPDs (from 0.25 to 7.5 mg) were added to 1 mL of Tris-HCl buffer (pH 7.4, 0.05 M). Then, different concentrations of Fe^{3+} aqueous solution (100 μL) were added to the above solution (900 μL), and the fluorescence spectra were recorded after incubation for 1 min. To investigate the selectivity of ssHPA-CPDs toward Fe^{3+} detection, different metal ions (Na^+, Ca^{2+}, Cu^{2+}, Zn^{2+}, Fe^{2+}, Mg^{2+}, Ag^+, Al^{3+}, CO_3^{2-}, NO_3^-, Cl^-, SO_4^{2-}, PO_4^{3-} to Fe^{3+}) with a final concentration of 300 μM were added into the standard sample to record the influence changes.

2.6. Biosafty of the ssHPA-CPDs

2.6.1. Cell cytotoxicity of ssHPA-CPDs

The MTT assay was employed to assess the cytotoxicity of ssHPA-CPDs on L929 cells, Caco-2 cells and HepG2 cells. After 24 h of culture in DMEM (37 °C, 5% CO_2), cells were plated in 96-well plates and exposed to different ssHPA-CPDs concentrations (0–1 mg/mL) for another 24 h. Next, 30 μL of MTT solution (5 mg/mL) was introduced into each well and incubated for 4 h. The insoluble crystals were subsequently solubilized with DMSO (100 μL/well) and homogenized by gentle pipetting. The absorbance at 570 nm was recorded to calculate the relative cell viability by using the formula:

Relative cell viability (%) = (OD_{sample} − OD_{blank}) / ($OD_{control}$ − OD_{blank}) × 100%.

2.6.2. Hemolytic activity testof ssHPA-CPDs

Red blood cells were collected by centrifuging the blood (1 mL) of Sprague-Dawley mice (SD, 4–6 week) at 1000 rpm for 5 min and then washing three times with 0.9% saline solution. The red blood cells were diluted 20 times before being co-incubated with the same volume of 0.9% saline solution (negative control), distilled water (positive control), and ssHPA-CPDs samples dissolved by saline solution with different concentrations (0.2 mg/mL, 0.3 mg/mL, 0.5 mg/mL, 0.75 mg/mL and 1.0 mg/mL), respectively. After 3 h at 37 °C, the mixture was centrifuged at 1000 rpm for 10 min, and the obtained supernatants were taken out for absorbance measurements at 545 nm. Each group was at least five times repeated. The hemolysis ratios were calculated using the following formula:

Hemolysis ratio (%) = (OD_{sample}-$OD_{negative}$) / ($OD_{positive}$-$OD_{negative}$) × 100%.

2.7. Fluorescent determination of Fe^{3+} ions in real samples

The microwave digestion method was employed to effectively convert solid food samples into a liquid state and oxidize various forms of bound iron to Fe^{3+} [27]. Specifically, meat by-products of pig liver, chicken liver, pig blood, and duck blood were first boiled for 5 min. 0.5 g of real sample was added to a mixed solution of concentrated nitric acid (5.0 mL) and 30% H_2O_2 (1.0 mL), followed by microwave digestion at 180 °C for 20 min. Subsequently, the digested solution was diluted to a final volume of 50 mL and adjusted to pH 7.4. For the real samples detection, 100 μL of diluted digested solution of real samples was combined with 900 μL of ssHPA-CPDs, incubated at 25 °C for 1 min, and then the emission spectrum of the solution was recorded under 350 nm excitation.

3. Results and discussion

3.1. Synthesis of ssHPA-CPDs

First, ssHPAs with flexible S—S bonds were successfully synthesized via a Michael addition reaction, and the content of S—S bonds was regulated by adjusting the ratio of monomer to polymerization. By verified from ^1H NMR, the CBA (with S—S bond) content in ssHPAs was successfully regulated from 0 to 100% (Fig. S1 and Table S1). Subsequently, the ssHPA-CPDs were obtained using CA (carbon source, 1.0 g) and ssHPAs (N/S source, 0.5 g) through the hydrothermal method, named $ssHPA_{x\%}$-CPDs (x = 0–100). The aqueous solution was chosen as the solvent because both ssHPA and CA are highly hydrophilic, allowing homogeneous precursor mixing. The aqueous hydrothermal environment moderates the carbonization process, promoting nonconjugated carbonized polymer dot formation and preserving disulfide-containing functional groups. The S content in $ssHPA_{x\%}$-CPDs ranged from 0.11% to 1.22%, indicating that the adjustment of the precursor material successfully modulated the levels of S doping in the ssHPA-CPDs (Table S2). Besides, the results indicate that as the yield of S atom in $ssHPA_{x\%}$-CPDs increases, the QY also increases from 25.00% to 29.08% (Fig. S2 and Table S3). Thus, $ssHPA_{100\%}$-CPDs were chosen for further experiment, and abbreviated as ssHPA-CPDs.

Subsequently, the ssHPA-CPDs synthesized at different reaction temperatures, heating times, and feed ratios of CA and $ssHPAs_{100\%}$ were measured to optimize the synthesis process. The results indicated that the emission intensity of the synthesized ssHPA-CPDs slightly increased with rising reaction temperature, reaching a peak at temperature above 130 °C (Fig. 1A). Besides, when the heating time exceeded 6 h, the fluorescence intensity of the ssHPA-CPDs plateaued (Fig. 1B). Taking into account energy efficiency and the fluorescence performance of the synthesized ssHPA-CPDs, the synthesis conditions were determined as 130 °C and 6 h. Furthermore, the ratio of CA (carbon source, 1.0 g) and $ssHPA_{100\%}$ (N/S source, from 0.04 g to 2.0 g) in the synthesis process of $ssHPA_{100\%}$-CPDs has also been optimized, and designated as ssHPA-CPD_x. The emission intensity varied significantly with changes in $ssHPA_{100\%}$ content, with ssHPA-$CPD_{0.5}$ displaying the highest PL intensity and ssHPA-$CPD_{0.04}$ showing the lowest (Fig. 1C). Based on these results, ssHPA-$CPD_{0.5}$ was selected for further application studies.

3.2. Characterization of ssHPA-CPDs

The morphology and size of the ssHPA-CPDs solutions are characterized by TEM. The results demonstrate that the creation of nearly monodisperse ssHPA-CPDs, exhibiting diameters ranging from 2.0 to 2.5 nm, which were uniformly distributed in solutions as spherical particles (Fig. 2, Fig. S3 and S4). HR-TEM images revealed distinct crystal fringes at a lattice spacing of 0.17–0.18 nm, corresponding to the diffraction planes of graphite carbon and aligning with the (102) plane of the graphite lattice, indicating that the ssHPA-CPDs have high crystallinity [28]. DLS analysis revealed that all ssHPA-CPDs formulations, regardless of the mass of ssHPA-CPDs increase from 0.04 to 2.0 g, the results exhibit a unimodal size distribution with hydrodynamic diameters centered range from 220 to 280 nm (Fig. S5). The negligible variation in particle size suggests that the polymer backbone, stabilized by disulfide crosslinking, reaches a consistent conformational state in aqueous solution.

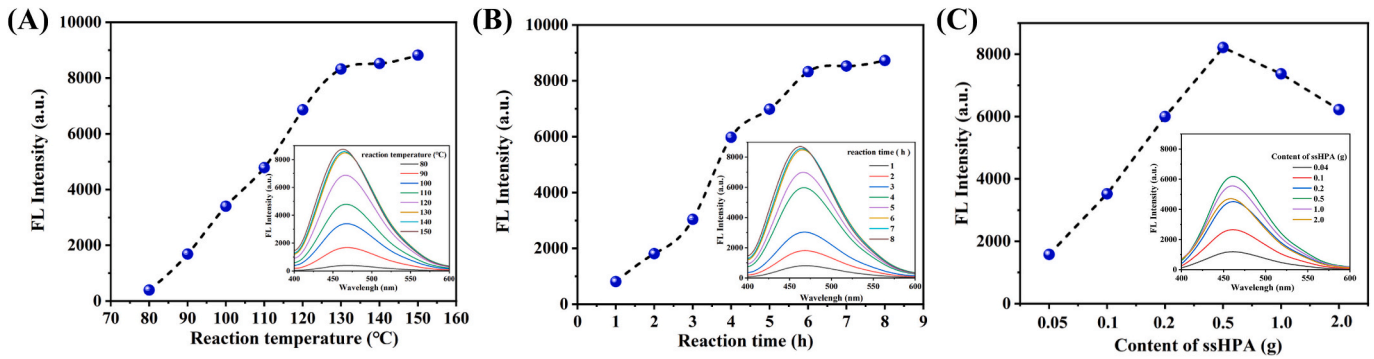

Fig. 1. Optimized synthesis conditions of ssHPA-CPD$_{0.5}$ in different reaction time (A), temperature (B) and content of ssHPA$_{100\%}$ (C).

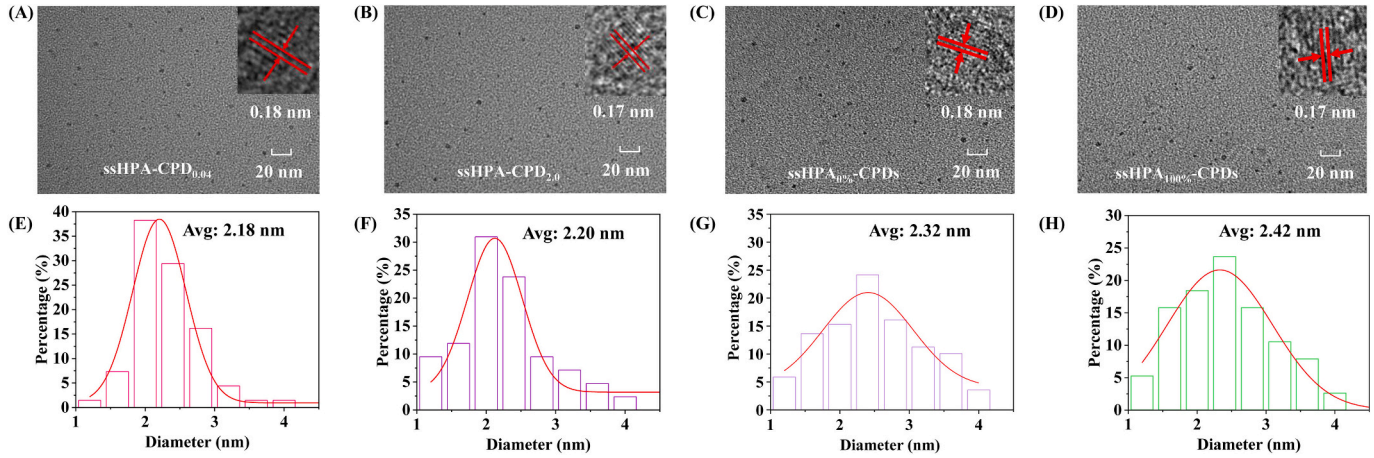

Fig. 2. (A)-(D) TEM image of different ssHPA-CPD$_x$ powder, (*E*)-(H) size of different ssHPA-CPD$_x$ solutions.

The SAXS analysis was used to characterize the morphology evolution and fractal interface of the ssHPA-CPD$_x$. Form factor fits to the

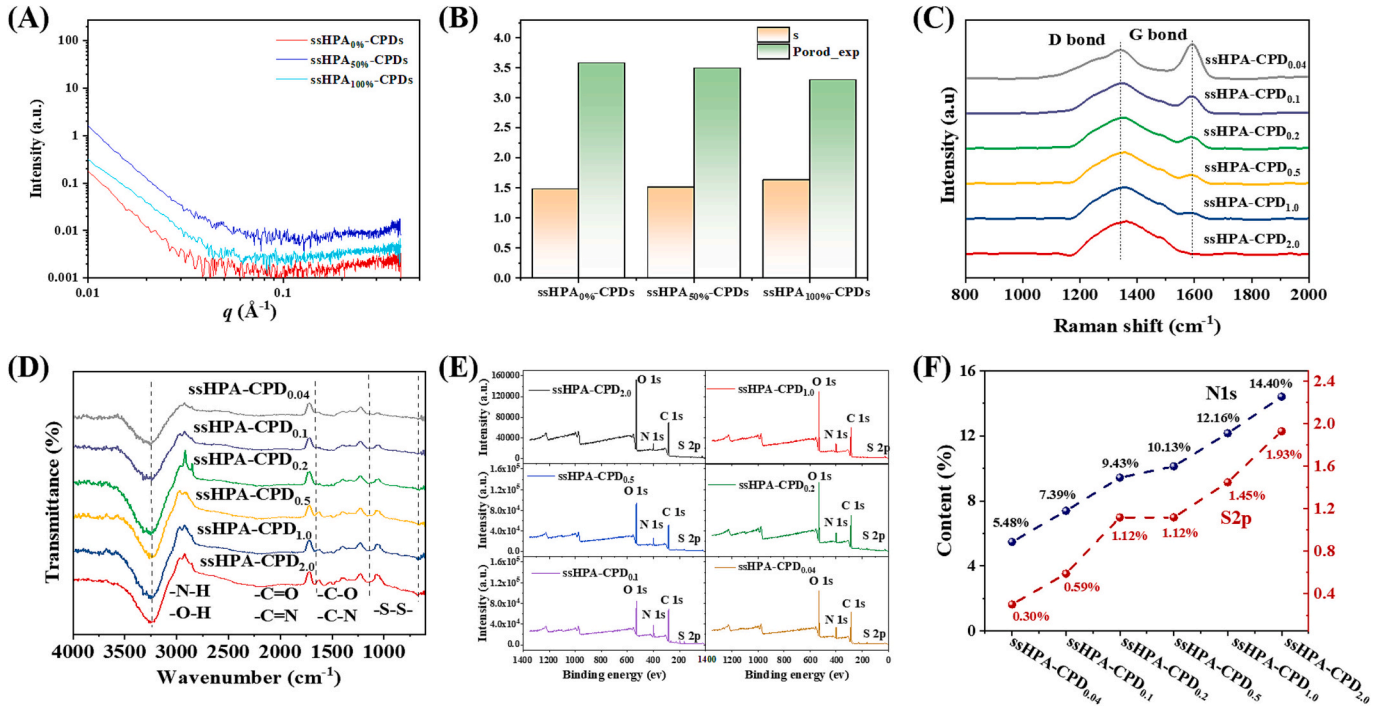

Fig. 3. (A)-(B) SAXS patterns of different ssHPA$_{x\%}$-CPD$_{0.5}$. (C) Raman spectroscopy, (D) FT-IR spectra, (E) full-range XPS spectra and (F) N and S content line diagram of different ssHPA-CPD$_x$.

scattering data were minimized using Levenberg−Marquardt nonlinear least-squares regression. Further estimation of parameter uncertainty was carried out using the DREAM algorithm (Markov Chain Monte Carlo sampling). The fitted power-law exponents reflect the morphological conformity of the ssHPA-CPD$_x$. For ideal spherical particles, s approaches 1. Besides, Porod_exp reflects the roughness of the interface, with an ideally smooth interface exhibiting a Porod_exp close to 4. From ssHPA$_{0\%}$-CPD$_{0.5}$ to ssHPA$_{100\%}$-CPD$_{0.5}$, remains nearly unchanged, and Porod_exp decreases (Fig. 3A and B). The results indicate that the flexibility of ssHPA-CPDs increases with higher disulfide bond content, resulting in greater surface roughness and a more irregular interface [29,30].

The degree of graphitization within the ssHPA-CPD$_x$ synthesized with different amounts of ssHPA$_{100\%}$ was determined using Raman spectroscopy. The intensity ratio of the D band to the G band (I_D/I_G) serves as a semi-quantitative indicator of the point defect density in the graphite structure. A higher I_D/I_G ratio suggests an increased number of defects or a more disordered arrangement within the carbon material. The results show that as the content of ssHPA$_{100\%}$ increases, the D band gradually increases, while the G band nearly vanishes (Fig. 3C). This indicates a transition from a phase dominated by larger sp^2 aromatic domains with few defects to one with more numerous sp^3 defects, ultimately leading to a more disordered phase of ssHPA-CPD$_x$ [31]. The FT-IR spectroscopy (Fig. 3D) revealed characteristic absorption bands for the ssHPA-CPD$_x$, including -OH and -NH stretching vibrations at 3200–3700 cm^{-1}, C═O stretching vibration at 1700 cm^{-1}, C═N and C-O/C-N stretching vibration at 1630 and 1150 cm^{-1}. Additionally, the peak at 600 cm^{-1} verifies the disulfide bonds formed from the reactant ssHPA [32,33].

By analyzing the entire XPS spectrum of ssHPA-CPD$_x$, the signals at 531.9 eV (O1s), 399.7 eV (N1s), 284.8 eV (C1s), and 163.3 eV (S2p) are observed (Fig. 3E). With the increasing concentration of the ssHPA$_{100\%}$, the N and S contents in the ssHPA-CPDx notably elevated, ranging from 5.48% to 14.4% for N atom and from 0.30% to 1.93% for S atom (Fig. 3F and Table S4).

Besides, the N1s spectrum reveals that the ssHPA-CPD$_x$ consist of graphitic nitrogen (~400.7 eV), pyrrolic nitrogen (~400.1 eV), and pyridinic nitrogen (~398.5 eV) species (Fig. 4 and Table S6) [34,35]. Spectral analysis indicated that graphitic nitrogen in ssHPA-CPD$_{0.5}$ constitutes the majority (82.22%) of the total N signal, with pyrrolic nitrogen contributing 16.11%. However, at very high or low ssHPA$_{100\%}$ concentrations, non-aromatic sp3-hybridized spacers, which do not form additional aromatic domains, became prevalent. Under these conditions, N predominantly remained in pyrrolic configurations. The high-resolution S2p spectrum indicates that the ssHPA-CPD$_x$ contain -S-S- (~164.0 eV), thiophenone/thiazole (~164.4 eV) and -C-S- (~163.5 eV) (Fig. S5 and Table S6) [36]. The highest content of thiophenone/thiazole is found in ssHPA-CPD$_{0.5}$, accounting for 24.73% of the total S signal.

The cytotoxicity of ssHPA-CPD$_{0.5}$ was evaluated through standard MTT assay using L929 cells, Caco-2 cells and HepG2 cells. Results revealed that cell viability remained above 80% when ssHPA-CPD$_{0.5}$ concentration reached 0.5 mg/mL (Fig. S7A-S7C). According to ISO 10993-5 criteria, materials are considered non-cytotoxic when relative cell viability maintains ≥70% of the blank control group. In the hemolytic activity assay, water and normal saline (ns) were used as positive and negative controls (Fig. S7B). After 4 h of incubation with red blood cells, the hemolysis ratios of ssHPA-CPD$_{0.5}$ concentrations within 0.5 mg/mL complies with the ASTM standard (<5%). These results demonstrate that ssHPA-CPDs exhibit low cytotoxicity and excellent blood compatibility, confirming the applicability for food component detection.

3.3. Optical properties of ssHPA-CPDs

The absorption spectra reveal that all prepared ssHPA-CPD$_x$ exhibit a prominent band around 250 nm, due to the π-π* transition in the aromatic hydrocarbon domains (Fig. 5A). Additionally, the short-wavelength features may arise from the absorption of σ bonds and individual aromatic rings, consistent with the phenomenon observed by Bhattacharyya, et al. [21]. The n-π* electronic transitions of the conjugated C═O and C═N groups are associated with the absorption peak at about 360 nm, and a weak shoulder at longer wavelengths (~ 600 nm) was attributed to the conjugated C═S bonding.

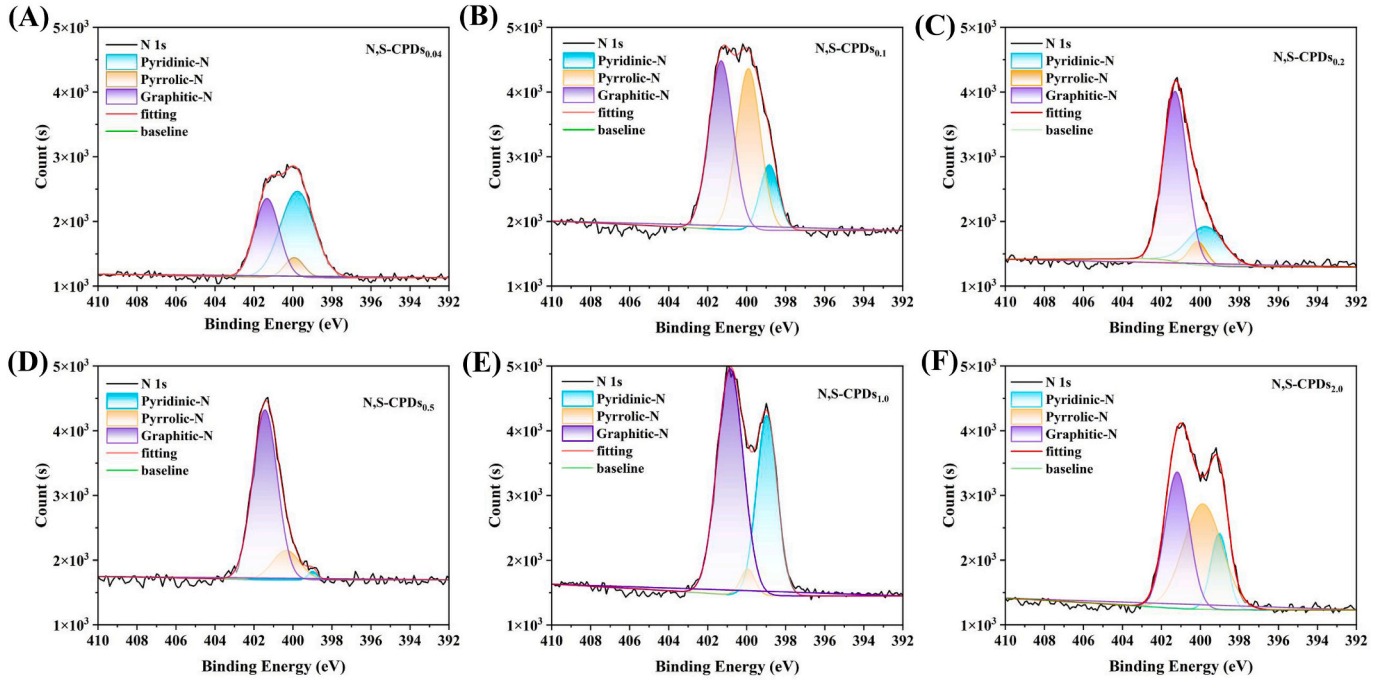

Fig. 4. High-resolution XPS spectra for nitrogen (N 1 s) of (A) ssHPA-CPD$_{0.04}$, (B) ssHPA-CPD$_{0.1}$,(C) ssHPA-CPD$_{0.2}$, (D) ssHPA-CPD$_{0.5}$ (E) ssHPA-CPD$_{1.0}$, (F) ssHPA-CPD$_{2.0}$.

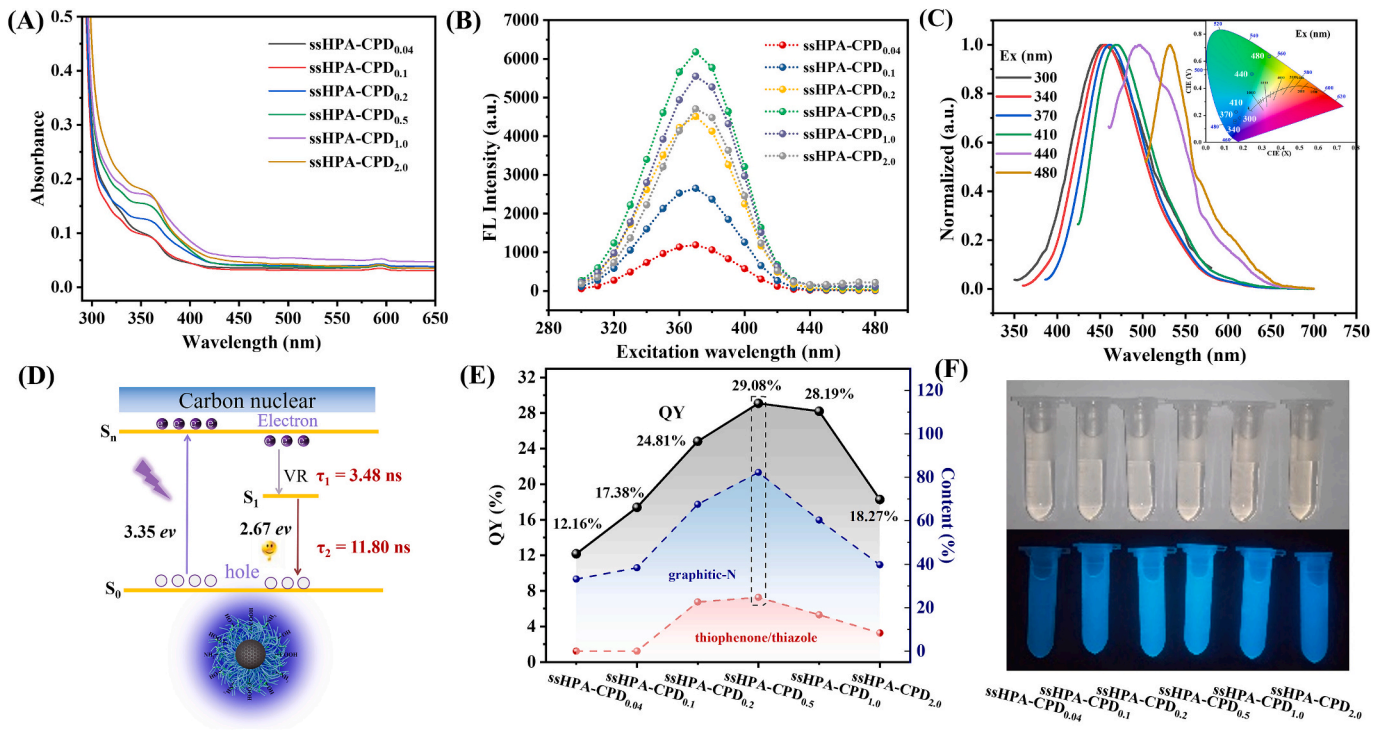

Fig. 5. (A) UV–Vis absorption spectra of ssHPA-CPDs, (B) fluorescence intensity of ssHPA-CPDs at different excitation wavelengths, (C) fluorescence spectra of ssHPA-CPD$_{0.5}$ at different excitation wavelengths (normalized), (D) fluorescence lifetime of ssHPA-CPDs and diagram of electronic energy level transitions and photon emission of ssHPA-CPD$_{0.5}$, (E) fluorescence quantum yield of ssHPA-CPDs, (F) photograph of ssHPA-CPDs under fluorescent and UV lamps.

The optical properties of ssHPA-CPD$_x$ were measured to investigate their relationship with the N and S doping levels. All samples exhibited similar PL spectra, with the emission peak located at 465 nm and a half-peak width of approximately 95 nm under the optimal excitation wavelength of 370 nm (Fig. 5B, Fig. S8). Furthermore, a plot shows the relationship between the excitation wavelength and emission peak position for ssHPA-CPD$_{0.5}$. Within the range of 330–480 nm, the emission peak exhibits a red shift as the excitation wavelength increases, confirming its excitation wavelength-dependent behavior (Fig. 5C). The fluorescence lifetime were calculated for ssHPA-CPD$_{0.04}$ ($\tau_1 = 10.70$ ns) to ssHPA-CPD$_{2.0}$ ($\tau_1 = 9.58$ ns), with ssHPA-CPD$_{0.5}$ exhibiting the longest fluorescence lifetime at 10.86 ns when monitored at 465 nm (Fig. 5D, Fig. S9 and Table S7).

Furthermore, the emission intensity of the ssHPA-CPD$_x$ at different concentrations was measured to calculate QY, using quinine sulfate as a standard (Fig. S10). When the amount of ssHPA$_{100\%}$ added during the reaction reached 0.5 g, the QY of ssHPA-CPD$_{0.5}$ reached a maximum value (29.08%), which is higher than that of CPDs prepared from commercial branched PEI without S—S bonds (8%). The results indicate that the strategy of doping S through introducing flexible S—S bonds significantly enhances the QY. Additionally, the results suggest that the QY of ssHPA-CPDs is also correlated with the amount of graphitic N and thiophene/thiazole S in the surface states and the carbon core, as supported by XPS data, which is consistent with the findings reported by Bhattacharyya, et al. [21] (Fig. 5E and F).

Three models of ssHPA-CPDs featuring a 150-atom hexacyclic aromatic architecture were constructed using DFT. The electron density and molecular orbitals indicated that ssHPA-CPD$_{0.5}$ exhibited the highest band gap of 1.08 eV. The reason can be attributed to the contribution of lone pair electrons from N or S atoms to the highest occupied molecular orbital (HOMO) of the CPDs. Additionally, graphite N embedded in the graphene lattice minimally disrupts conjugation structure, while serving as an effective electron donor, also increasing the band gap. However, a reduced band gap (0.69 eV) of ssHPA-CPD$_{2.0}$ appears, as excessive N doping disrupts the sp^2 conjugated structure of CPDs, introducing more defects, distortions, and amorphous regions (Fig. S11). Although an increased band gap would typically induce a blue shift of fluorescence emission, the emission wavelengths of ssHPA-CPDs show minimal variation. This observation suggests that the PL mechanism in these CPDs is not solely governed by the HOMO-LUMO transition, but may also involve fluorescent moieties (e.g., C═O and C═N groups) present in partially carbonized polymer segments.

Additionally, the fluorescence properties of ssHPA-CPD$_{0.5}$ stored at a 4 °C refrigerator were monitored over 30 days, and the fluorescence intensity remained stable throughout the duration, with no notable quenching or enhancement, as illustrated in Fig. S12. Meanwhile, the fluorescence intensity of ssHPA-CPD$_{0.5}$ under continuous excitation has been measured at multiple time points. The results indicate that the fluorescence intensity of ssHPA-CPD$_{0.5}$ keep stable during the continuous excitation in 120 min, it remains at a high level (Fig. S13). The above results demonstrate the excellent fluorescence stability of the ssHPA-CPDs sensors.

3.4. Fe^{3+} sensing properties of ssHPA-CPDs

As a Fe^{3+}-responsive fluorescent sensor, the emission intensity of ssHPA-CPD$_{0.5}$ significantly decreased after reacting with Fe^{3+} ions, demonstrating the feasibility of using ssHPA-CPDs (Fig. 6A). To determine the optimal detection conditions for the fluorescent sensor, the effects of pH values, solvent system and probe concentrations on the quenching efficiency $(F—F_0)/F_0$ of ssHPA-CPDs after reacting with Fe^{3+} ions were studied. The results show that the fluorescence of ssHPA-CPD$_{0.5}$ remained stable within pH 3 to 11, with minimal variation in Fe^{3+} ions quenching efficiency (Fig. 6B). Considering physiological relevance and enhancing the practical applicability of the probe, pH 7.4 was selected. As shown in Fig. S13, the fluorescent spectrum and quenching efficiency almost the same both in pure water and Tris-HCl (pH 7.4) buffer. Within a certain range, a higher concentration of ssHPA-CPD$_{0.5}$ solution results in stronger fluorescence intensity (Fig. 6C), while the quenching efficiency of Fe^{3+} ions gradually

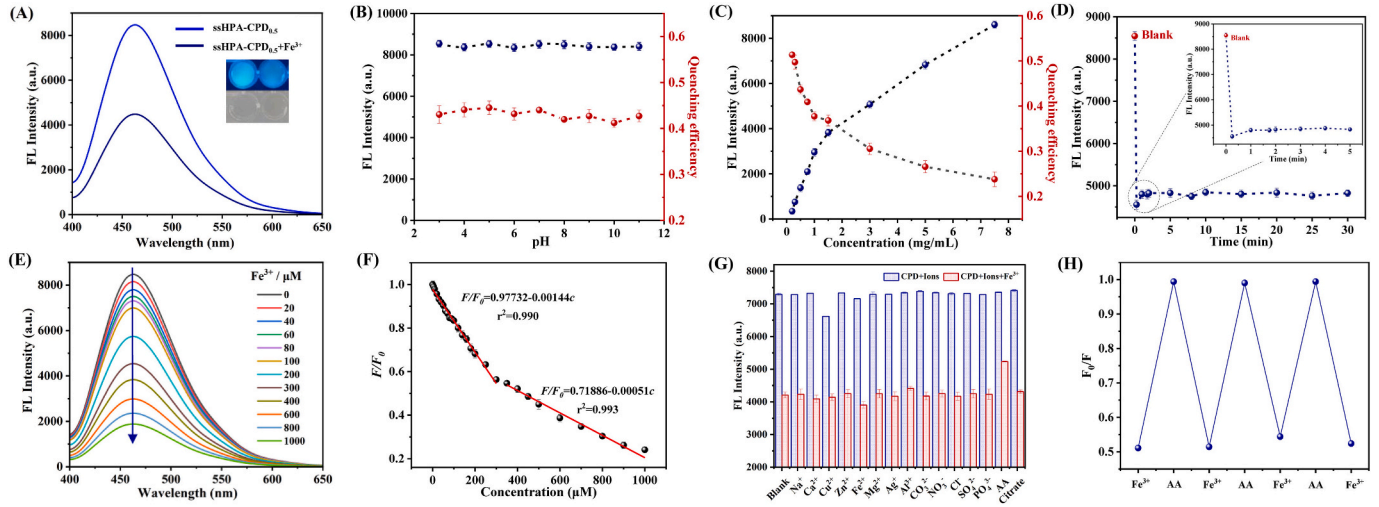

Fig. 6. (A) Fluorescence response of ssHPA-CPD$_{0.5}$ to Fe^{3+}, optimization of detection conditions, (B) pH of the detection system, (C) concentration of ssHPA-CPD$_{0.5}$, (D) detection time, (E) different concentrations of Fe^{3+}, (F) linear relationship between the concentration of Fe^{3+} and the relative fluorescence intensity (F/F_0) of ssHPA-CPD$_{0.5}$, (G) selectivity and anti-interference of ssHPA-CPD$_{0.5}$ for different analytes (blue bars represent the response of ssHPA-CPD$_{0.5}$ to different substances, while the red bars represent the response of ssHPA-CPD$_{0.5}$ to different substances in the presence of Fe^{3+}, (H) fluorescence intensity changes of ssHPA-CPD$_{0.5}$ after the addition of Fe^{3+} (300 μM) and AA (1 mM). (For interpretation of the references to colour in this figure legend, the reader is referred to the web version of this article.)

decreases. Thus, 0.5 mg/mL of ssHPA-CPD$_{0.5}$ was selected as the optimal concentration. Subsequently, the response characteristics of ssHPA$_{x}$ $_{\%}$-CPDs with different S—S contents to Fe^{3+} ions were also investigated (Fig. S14). The results demonstrated that ssHPA$_{100\%}$-CPDs exhibited the most pronounced fluorescence response to Fe^{3+} ions, indicating that S atom incorporation not only modulated the PL properties of the CPDs but also enhanced their binding affinity for Fe^{3+} ions. Furthermore, Fig. 6D illustrates the changes in the fluorescent response of the ssHPA-CPD$_{0.5}$ over time after reacting with Fe^{3+}. The results indicate that the fluorescence quenching behavior is rapidly completed within 1 min and remains stable for at least 30 min.

Under optimal detection conditions, the changes in emission intensity of ssHPA-CPD$_{0.5}$ after responsing of Fe^{3+} ions were measured. The results show that the emission of ssHPA-CPD$_{0.5}$ gradually decreased with the increasing concentration of Fe^{3+} ions (Fig. 6E). The limit of detection (LOD) is calculated as 0.07 μM according to the LOD = 3σ/slope, where σ is the standard deviation of 20 samples, and slope is obtained from the calibration curve (Table S8). As shown in Fig. 6F, the F/F_0 values exhibita a biphasic linear response, a low-concentration segment from 0 to 300 μM and a high-concentration segment from 300 to 1000 μM with R^2 all above 0.99. This broad linear range of 0–1000 μM encompasses nutritional (11–27 μM), clinical (>30 μM), and toxicologically (>440 μM) relevant iron concentrations [37,38]. Compared to other methods for detecting Fe^{3+} ions, this method offers a relatively wide detection range (0–1000 μM), a lower detection limit (0.07 μM), and a higher quantum yield (29.08%) (Table S9).

In addition, the interference of other interfering substances, including Na^+, Ca^{2+}, Cu^{2+}, Zn^{2+}, Fe^{2+}, Mg^{2+}, Ag^+, Al^{3+}, CO_3^{2-}, NO_3^-, Cl^-, SO_4^{2-}, PO_4^{3-}, AA, and citrate to Fe^{3+} ions was measured. The interfering substances were separately mixed with the ssHPA-CPD$_{0.5}$, with a final concentration of 300 μM for each. The results indicate that the emission of the ssHPA-CPD$_{0.5}$ remained unaffected by these substances. The mixture of ssHPA-CPD$_{0.5}$ with interfering substances was also tested to assess their potential interference in Fe^{3+} ion detection. With the exception of AA, the presence of other coexisting substances did not significantly interfere with the Fe^{3+} induced fluorescence quenching of ssHPA-CPD$_{0.5}$ (Fig. 6G). This underscores the exceptional selectivity of the ssHPA-CPDs for Fe^{3+} ion detection over other typical inorganic ions. However, The addition of AA markedly suppressed the fluorescence quenching effect of Fe^{3+} on ssHPA-CPD$_{0.5}$, which can be attributed to its ability to reduce Fe^{3+} to Fe^{2+} [39]. Therefore, the recyclability of ssHPA-CPDs was confirmed by adding AA into the ssHPA-CPD$_{0.5}$/Fe^{3+} complex. Specifically, the fluorescence intensity decreases sharply upon adding Fe^{3+} ions, and reaches equilibrium within 1 min. Furthermore, the fluorescence intensity could be restored approximately 1 min after the addition of an AA solution, with relative standard deviations (RSD) about 0.42% across cycles. Over three cycles of adding Fe^{3+}/AA, the fluorescence intensity demonstrated excellent recyclability (Fig. 6H). Notably, three independently synthesized batches of ssHPA-CPD$_{0.5}$ were prepared under identical conditions and tested for their fluorescence response toward Fe^{3+} (300 μM). The results showed the fluorescent signals with RSD below 5% across batches (Fig. S15).

3.5. *Fe^{3+} sensing mechanism of ssHPA-CPDs*

To further understand the mechanism of fluorescence quenching of ssHPA-CPD$_{0.5}$ induced by Fe^{3+}, the ζ potential of ssHPA-CPDs was evaluated. As depicted in Fig. 7A, the ζ potential increased from 1.18 mV to 22.50 mV following the interaction with Fe^{3+} ions, confirming the coordination interaction between Fe^{3+} ions and the -OH, -COOH, and -NH_2 groups of the ssHPA-CPD$_{0.5}$ [40]. Additionally, the fluorescence lifetime of the ssHPA-CPD$_{0.5}$ was measured in the presence and absence of Fe^{3+} ions (Fig. 7B). The results show that the fluorescence lifetime remains nearly unchanged before and after incubation with Fe^{3+}, which is the direct indicator of static quenching. Meanwhile, the UV–Vis absorption spectrum of ssHPA-CPD$_{0.5}$ also shows significant changes at an Fe^{3+} concentration of 1000 μM. Moreover, precipitation occurs only when the Fe^{3+} ions are present in large excess (>2000 μM), which further substantiates the complex formation due to the specific coordination interactions between Fe^{3+} and the carboxyl and amino functional groups on the surface of ssHPA-CPDs (Fig. 7C). The formation of non-fluorescent complexes between fluorophores and Fe^{3+} in the ground state doesn't alter the fluorescence lifetime of uncomplexed fluorophores but induces significant changes in the absorption spectrum, which confirming that the quenching process is static [41]. Moreover, a partial overlap between the absorption spectrum of Fe^{3+} and the excitation spectrum of ssHPA-CPDs was observed, indicating that the inner filter effect may contribute to the fluorescence quenching process (Fig. S16). The increase in thiol content after Fe^{3+} ion interaction suggests that the oxidative nature of Fe^{3+} may cause structural fragmentation of the ssHPA-CPD$_{0.5}$, facilitating complex formation (Fig. S17).

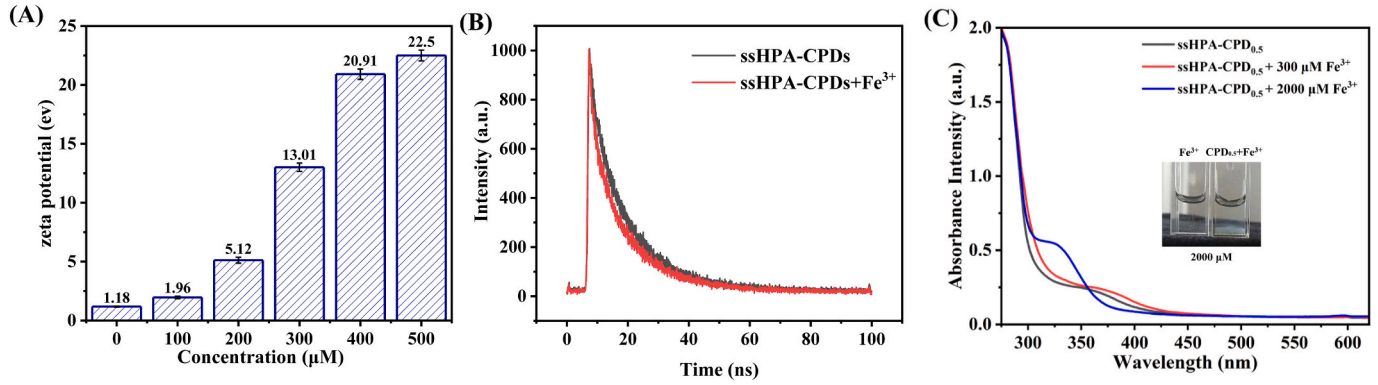

Fig. 7. Changes in (A) zeta potential, (B) fluorescence lifetime, and (C) UV–Vis absorption patterns of ssHPA-CPD$_{0.5}$ after Fe^{3+} addition.

3.6. Analysis of real samples

The Fe element is rich in liver and blood, which have the benefits of replenishing energy and calming the mind. The Fe content in liver and blood also represents an important indicator of metabolic diseases [42,43]. Therefore, the rapid and accurate quantification of Fe content in liver and blood samples is of great necessity.

By using microwave digestion, the Fe element in actual samples of blood and liver can be oxidised to Fe (III), enabling the ssHPA-CPDs to detect the total Fe levels, which can be detected reliably and stably through ssHPA-CPD$_{0.5}$. The measured contents of Fe^{3+} in pig liver, chicken liver, duck blood, and pig blood were 18.12, 18.52, 21.64, and 21.90 mg/100 g (wet weight), respectively. The Fe(III) contents determined in animal liver and blood products are within the range reported in previous studies (typically 15–30 mg/100 g) [44,45], indicating the biological relevance and practical applicability of the proposed sensing strategy. As shown in Table 1, the method demonstrated good recovery rates (ranging from 87.47% to 106.01%) and low relative standard deviations (< 3.5%) ($n = 3$). In addition, the results obtained by the proposed method were compared with those measured by inductively coupled plasma mass spectrometry (ICP-MS) as a reference method. The absolute deviations between the two methods below 1.8 mg/100 g, corresponding to relative deviations within 8%. The recovery rates obtained by ICP-MS ranged from 96.09% to 109.24%, which are comparable to the method of ssHPA-CPD$_{0.5}$. These findings indicate that ssHPA-CPD$_{0.5}$ provides analytical performance equivalent to that of ICP-MS, while offering advantages such as simplicity and rapidity for routine iron monitoring in food samples.

4. Conclusion

A flexible disulfide-bridged hyperbranched poly(amido amine)s based nonconjugated carbonized polymer dots was successfully synthesized. The incorporation of disulfide bonds into the ssHPA-CPDs varies depending on the precursor of ssHPA present during synthesis. When the mass ratio of ssHPA-CPDs/citric acid is 0.5, graphite nitrogen and thiophenone/thiazole sulfur in ssHPA-CPD$_{0.5}$ occupy a dominant position, with a higher quantum yield (29.08%), along with the doping ratios of nitrogen and sulfur are 10.13% and 1.22%, respectively. The flexibility of ssHPA-CPDs increases with higher disulfide bond content, resulting in greater surface roughness and a more irregular interface. The obtained ssHPA-CPDs were characteristic of Fe^{3+}-responsive fluorescence emission. The Fe^{3+} concentration exhibited a good linear relationship with the fluorescence ratio (F_0/F) of the ssHPA-CPDs, achieving a LOD of 0.07 μM. This method offers a rapid (1 min), accurate ($R^2 = 0.99$), and low-cost detection approach for detecting Fe content in liver and blood samples with good recovery rates (87.47%–106.01%), reproducibility (RSD < 3.5%) , and recyclability (~5 times).

Table 1
Detection of Fe^{3+} in real samples.

Method	Sample	Found/(mg/100 g)	Added/(mg/100 g)	Found/(mg/100 g)	Recovery/%	RSD/%
ssHPA-CPD$_{0.5}$	pig liver	18.12 ± 0.24	10.0	27.67 ± 0.13	98.21	0.47
			20.0	35.57 ± 1.13	93.07	3.17
			30.0	44.43 ± 1.28	92.05	2.9
	chicken liver	18.52 ± 0.15	10.0	30.28 ± 0.10	106.01	0.34
			20.0	34.77 ± 1.03	90.04	2.98
			30.0	49.67 ± 1.10	102.08	2.21
	pig blood	21.64 ± 0.42	10.0	29.53 ± 0.05	93.2	0.16
			20.0	36.51 ± 0.96	87.47	2.64
			30.0	51.23 ± 1.24	98.93	2.42
	duck blood	21.90 ± 0.45	10.0	33.35 ± 0.14	104.39	0.43
			20.0	40.87 ± 0.94	97.30	2.31
			30.0	46.20 ± 0.77	88.76	1.67
ICP-MS	pig liver	19.54 ± 0.35	10.0	30.57 ± 0.31	106.77	1.01
			20.0	41.23 ± 1.21	105.61	2.93
			30.0	52.89 ± 1.45	109.24	2.74
	chicken liver	18.23 ± 0.22	10.0	27.98 ± 0.19	99.12	0.68
			20.0	37.45 ± 0.78	97.45	2.08
			30.0	47.89 ± 1.05	99.30	2.19
	pig blood	21.12 ± 0.38	10.0	30.67 ± 0.23	98.56	0.75
			20.0	39.89 ± 0.88	96.09	2.21
			30.0	49.34 ± 1.15	96.53	2.33
	duck blood	23.78 ± 0.52	10.0	31.23 ± 0.18	99.30	0.58
			20.0	40.67 ± 0.82	97.65	2.02
			30.0	50.12 ± 1.08	97.42	2.16

This work introduces a new strategy to modulate the backbone flexibility by controllably introducing disulfide bonds into hyperbranched polymers for Fe (III) detection. Combined with a fluorescence-based backpropagation neural network model, an accuracy rate of 100% was achieved, offering a promising approach for monitoring Fe (III) in the food analysis and biomedical field.

Declaration of competing interest

The authors declare that they have no known competing financial interests or personal relationships that could have appeared to influence the work reported in this paper.

Acknowledgments

This work was financially supported by the National Key Research and Development Program of China (2021YFD1600705), and Agriculture Research System of China of MOF and MARA CARS-38.

Appendix A. Supplementary data

Supplementary data to this article can be found online at https://doi.org/10.1016/j.saa.2026.127837.

Data availability

Data will be made available on request.

References

[1] H. Shin, F. Jannah, E.J. Yoo, J.-M. Kim, A colorimetric and fluorescence “turn-on” sensor for Fe(III) ion based on imidazole-functionalized polydiacetylene, Sensors Actuators B Chem. 350 (2022) 130885, https://doi.org/10.1016/j.snb.2021.130885.

[2] R. Zhou, M. Dong, Y. Wu, Rapid, visual and autocatalytic quantifying ag(I) and Fe (III) by ratiometric fluorescence sensor of n, si, S-GQDs/OPD, Spectrochim. Acta A 340 (2025) 126366, https://doi.org/10.1016/j.saa.2025.126366.

[3] D.N. Perera, C.L. Palliyaguruge, D.D. Eapasinghe, D.M. Liyanage, R.A.C. H. Seneviratne, S.M.D. Demini, J.A.S.M. Jayasinghe, M. Faizan, U. Rajagopalan, B. P. Galhena, H. Hays, K. Senathilake, K.H. Tennekoon, S.R. Samarakoon, Factors affecting iron absorption and the role of fortification in enhancing iron levels, Nutr. Bull. 48 (4) (2023) 442–457, https://doi.org/10.1111/nbu.12643.

[4] Y. Man, T. Xu, B. Adhikari, C. Zhou, Y. Wang, B. Wang, Iron supplementation and iron-fortified foods: a review, Crit. Rev. Food Sci. Nutr. 62 (16) (2022) 4504–4525, https://doi.org/10.1080/10408398.2021.1876623.

[5] B.R. Bacon, C.H. Park, G.M. Brittenham, R. O-Neill, A.S. Tavill, Hepatic mitochondrial oxidative metabolism in rats with chronic dietary iron overload, Hepatology 5 (5) (1985), https://doi.org/10.1002/hep.1840050514.

[6] H. Song, S. Zhang, X. Sun, J. Liu, Y. Wu, W. Guo, F. Wang, X. Ou, M. Cong, E. Jin, W. Li, S. Liu, Distinct iron deposition profiles of liver zones in various models with iron homeostasis disorders, Adv. Sci. 5 (11) (2018) 1800866, https://doi.org/10.1002/advs.201800866.

[7] K. Shubham, T. Anukiruthika, S. Dutta, A.V. Kashyap, J.A. Moses, C. Anandharamakrishnan, Iron deficiency anemia: a comprehensive review on iron absorption, bioavailability and emerging food fortification approaches, Trends Food Sci. Technol. 99 (2020) 58–75, https://doi.org/10.1016/j.tifs.2020.02.021.

[8] Y. Huang, D. Cao, Z. Chen, B. Chen, J. Li, R. Wang, J. Guo, Q. Dong, C. Liu, Q. Wei, L. Liu, Iron intake and multiple health outcomes: umbrella review, Crit. Rev. Food Sci. Nutr. 63 (16) (2023) 2910–2927, https://doi.org/10.1080/10408398.2021.1982861.

[9] E. Charlebois, K. Pantopoulos, Nutritional aspects of iron in health and disease, Nutrients 15 (11) (2023) 2441, https://doi.org/10.3390/nu15112441.

[10] T. Martinez, I. Carlos, M. Leets, M. Layrisse Renzi, Iron absorption by humans from veal liver1, J. Nutr. 104 (8) (1974) 983–993, https://doi.org/10.1093/jn/104.8.983.

[11] C. Berraquero-García, M.C. Almécija, E.M. Guadix, R. Pérez-Gálvez, Valorisation of blood protein from livestock to produce haem iron-fortified hydrolysates with antioxidant activity, Int. J. Food Sci. Technol. 57 (4) (2022) 2479–2486, https://doi.org/10.1111/ijfs.15616.

[12] Z.S. Kardar, F. Shemirani, R. Zadmard, Determination of iron(II) and iron(III) via static quenching of the fluorescence of tryptophan-protected copper nanoclusters, Microchim. Acta 187 (1) (2020) 81, https://doi.org/10.1007/s00604-019-4067-4.

[13] S. Pawar, H. Duadi, M. Friedman Gohas, Y. Cohen, D. Fixler, Bioimaging based on poly(ethylenimine)-coated carbon dots and gold nanoparticles for pH sensing and metal enhanced fluorescence, ACS Appl. Bio Mater. 6 (11) (2023) 4935–4943, https://doi.org/10.1021/acsabm.3c00639.

[14] Z. Mu, J. Hua, S. Feng, Y. Yang, A ratiometric fluorescence and light scattering sensing platform based on cu-doped carbon dots for tryptophan and Fe(III), Spectrochim. Acta A 219 (2019) 248–256, https://doi.org/10.1016/j.saa.2019.04.065.

[15] Y. Han, B. Rui, Y. Jianhong, H. Li, L. Liu, S. Huang, Z. Li, W. Zhang, D. Min, One-step synthesis of tungsten-doped carbonated polymer dots with high sensitivity to fe (III) and pH environments, Mater. Today Commun. 34 (2023) 105317, https://doi.org/10.1016/j.mtcomm.2023.105317.

[16] J. Xia, Y. Zhuang, Y. Yu, J. Wang, Highly fluorescent carbon polymer dots prepared at room temperature, and their application as a fluorescent probe for determination and intracellular imaging of ferric ion, Microchim. Acta 184 (4) (2017) 1109–1116, https://doi.org/10.1007/s00604-017-2104-8.

[17] J. Yin, H. Liu, S. Jiang, Y. Chen, Y. Yao, Hyperbranched polymer functionalized carbon dots with multistimuli-responsive property, ACS Macro Lett. 2 (11) (2013) 1033–1037, https://doi.org/10.1021/mz400474v.

[18] L. Guo, H. Yan, L. Yan, L. Bai, S. Niu, Y. Zhao, A hyperbranched polysiloxane containing carbon dots with near white light emission, Polym. Chem. 12 (24) (2021) 3582–3591, https://doi.org/10.1039/D1PY00430A.

[19] Y. Qiao, L. Guo, Y. He, Z. Li, Q. Meng, J. Yao, Y. Zhao, H. Yan, Dual-excitation and single-emission b, n-codoped carbon dots: synthesis, fluorescent properties and multi-ion detection, J. Photochem. Photobiol., A 462 (2025) 116180, https://doi.org/10.1016/j.jphotochem.2024.116180.

[20] S. Zhu, L. Wang, N. Zhou, X. Zhao, Y. Song, S. Maharjan, J. Zhang, L. Lu, H. Wang, B. Yang, The crosslink enhanced emission (CEE) in non-conjugated polymer dots: from the photoluminescence mechanism to the cellular uptake mechanism and internalization, Chem. Commun. 50 (89) (2014) 13845–13848, https://doi.org/10.1039/C4CC05806B.

[21] S. Bhattacharyya, F. Ehrat, P. Urban, R. Teves, R. Wyrwich, M. Döblinger, J. Feldmann, A.S. Urban, J.K. Stolarczyk, Effect of nitrogen atom positioning on the trade-off between emissive and photocatalytic properties of carbon dots, Nat. Commun. 8 (1) (2017) 1401, https://doi.org/10.1038/s41467-017-01463-x.

[22] X. Li, S. Zhao, B. Li, K. Yang, M. Lan, L. Zeng, Advances and perspectives in carbon dot-based fluorescent probes: mechanism, and application, Coord. Chem. Rev. 431 (2021) 213686, https://doi.org/10.1016/j.ccr.2020.213686.

[23] X. Kou, S. Jiang, S.-J. Park, L.-Y. Meng, A review: recent advances in preparations and applications of heteroatom-doped carbon quantum dots, Dalton Trans. 49 (21) (2020) 6915–6938, https://doi.org/10.1039/D0DT01004A.

[24] C. Yan, X. Shao, Y. Wang, S. Tang, S. Li, C. Wang, M. Bai, Y. Qi, Y. Ma, R. Zhao, W. Zhu, J. Shi, S. Ding, Z. Lyu, Application of carbon dots-based nanomaterials in amyloid aggregation disease, Carbon 234 (2025) 119971, https://doi.org/10.1016/j.carbon.2024.119971.

[25] J. Tian, M. An, X. Zhao, Y. Wang, M. Hasan, Advances in fluorescent sensing carbon dots: An account of food analysis, ACS Omega 8 (10) (2023) 9031–9039, https://doi.org/10.1021/acsomega.2c07986.

[26] C. Li, Y. Chen, L. Yang, C. Zhang, B. Wang, Y. Wang, Tetraphenylethene decorated hyperbranched poly(amido amine)s as metal/organic-solvent-free turn-on AIE probe for specific pyrophosphate detection, Sensors Actuators B Chem. 291 (2019) 25–33, https://doi.org/10.1016/j.snb.2019.04.056.

[27] Y. Chen, H. Zhang, Y. Li, T. Wang, Pterostilbene confers protection against Diquat-induced intestinal damage with potential regulation of redox status and ferroptosis in broiler chickens, Oxidative Med. Cell. Longev. 2023 (1) (2023) 8258354, https://doi.org/10.1155/2023/8258354.

[28] H. Kang, H. Geng, S. Shi, Z. Song, Y. Dong, X. Yan, C. Wang, Y. Mao, Q. Cai, CuInS2/ZnS QDs-based fluorescent probe for detection of cu2+, Prog. Nat. Sci.: Mater. Int. 33 (4) (2023) 495–500, https://doi.org/10.1016/j.pnsc.2023.08.011.

[29] M. Herbst, E. Hofmann, S. Förster, Nucleation and growth kinetics of ZnO nanoparticles studied by in situ microfluidic SAXS/WAXS/UV–vis experiments, Langmuir 35 (36) (2019) 11702–11709, https://doi.org/10.1021/acs.langmuir.9b01149.

[30] K.P. Barteau, K. Ma, F.F.E. Kohle, T.C. Gardinier, P.A. Beaucage, R.E. Gillilan, U. Wiesner, Quantitative measure of the size dispersity in ultrasmall fluorescent organic–inorganic hybrid core–shell silica nanoparticles by small-angle X-ray scattering, Chem. Mater. 31 (3) (2019) 643–657, https://doi.org/10.1021/acs.chemmater.8b04369.

[31] M.H. Nguyen, D.T. Le, H.T. Do, A.T. Le, Remarkable luminescent carbon quantum dots: green synthesis from orange juice using microplasma-liquid method, Fullerenes Nanotubes Carbon Nanostruct. 32 (3) (2024) 282–287, https://doi.org/10.1080/1536383X.2023.2274917.

[32] S. Bhattacharya, R.S. Phatake, S. Nabha Barnea, N. Zerby, J.-J. Zhu, R. Shikler, N. G. Lemcoff, R. Jelinek, Fluorescent self-healing carbon dot/polymer gels, ACS Nano 13 (2) (2019) 1433–1442, https://doi.org/10.1021/acsnano.8b07087.

[33] N. Thakur, B. Singh, Designing protein-polysaccharides based bioactive copolymeric network by supra-molecular interactions for sustained drug delivery, Supramol. Mater. 2 (2023) 100048, https://doi.org/10.1016/j.supmat.2023.100048.

[34] S. Chandra, D. Bano, K. Sahoo, D. Kumar, V. Kumar, P. Kumar Yadav, S. Hadi Hasan, Synthesis of fluorescent carbon quantum dots from jatropha fruits and their application in fluorometric sensor for the detection of chlorpyrifos, Microchem. J. 172 (2022) 106953, https://doi.org/10.1016/j.microc.2021.106953.

[35] A. Kumar, S. Barala, A.P. Gutal, A.G. Chakkar, P. Kumar, M. Paranjothy, M. Kumar, Silver-atom catalysts boosted nitrogen-doped MoS_2 for chemiresistive NO_2 gas sensor, Sensors Actuators B Chem. 439 (2025) 137839, https://doi.org/10.1016/j.snb.2025.137839.

[36] X. Zhu, Y. Zhang, Z. Ma, Y. He, P. Song, R. Wang, Construction of thiazole-zwitterionic copolymer nanospheres with iso-bifunctional groups for excellent

antibacterial activity, Prog. Org. Coat. 186 (2024) 108084, https://doi.org/10.1016/j.porgcoat.2023.108084.
[37] C. Hershko, Pathogenesis and management of iron toxicity in thalassemia, Ann. N. Y. Acad. Sci. 1202 (2010) 1–9, https://doi.org/10.1111/j.1749-6632.2010.05544.x.
[38] R.F. Ritchie, G.E. Palomaki, L.M. Neveux, O. Navolotskaia, T.B. Ledue, W.Y. Craig, Reference distributions for serum iron and transferrin saturation: a practical, simple, and clinically relevant approach in a large cohort, J. Clin. Lab. Anal. 16 (5) (2002) 237–245, https://doi.org/10.1002/jcla.10048.
[39] Y.H.P. Hsieh, Y.P. Hsieh, Valence state of iron in the presence of ascorbic acid and ethylenediaminetetraacetic acid, J. Agric. Food Chem. 45 (4) (1997) 1126–1129, https://doi.org/10.1021/jf960684n.
[40] D. Chang, Z. Zhao, W. Niu, L. Shi, Y. Yang, Iron ion sensing and in vitro and in vivo imaging based on bright blue-fluorescent carbon dots, Spectrochim. Acta A 260 (2021) 119964, https://doi.org/10.1016/j.saa.2021.119964.
[41] S. Rajendran, D.V. Ramanaiah, S. Kundu, S.K. Bhunia, Yellow fluorescent carbon dots for selective recognition of as3+ and fe3+ ions, ACS Appl. Nano Mater. 4 (10) (2021) 10931–10942, https://doi.org/10.1021/acsanm.1c02391.
[42] C. Cheng, L. Chen, D. Zhang, J. Yu, M. Zhu, C. Li, X. Zheng, C. Blecker, S. Li, Value-added utilization of hemoglobin and its hydrolysis products from livestock and poultry blood processing by-products: a review, Trends Food Sci. Technol. 151 (2024) 104645, https://doi.org/10.1016/j.tifs.2024.104645.
[43] A. Latoch, D.M. Stasiak, P. Siczek, Edible offal as a valuable source of nutrients in the diet—a review, Nutrients 16 (11) (2024) 1609, https://doi.org/10.3390/nu16111609.
[44] C.E. Carpenter, E. Clark, Evaluation of methods used in meat iron analysis and iron content of raw and cooked meats, J. Agric. Food Chem. 43 (7) (1995) 1824–1827, https://doi.org/10.1021/jf00055a014.
[45] I.M. Oellingrath, E. Slinde, Color, pigment and iron content of meat loaves with blood, blood emulsion, or mechanically deboned meat added, J. Food Sci. 50 (6) (1985) 1551–1555, https://doi.org/10.1111/j.1365-2621.1985.tb10531.x.